Gravity waves in the middle atmosphere observed by Rayleigh lidar: 1. Case studies

Richard Wilson, Marie-Lise Chanin, Alain Hauchecorne

JOURNAL OF GEOPHYSICAL RESEARCH, VOL. 96, NO. D3, PAGES 5153–5167, MARCH 20, 1991

GRAVITY WAVES IN THE MIDDLE ATMOSPHERE OBSERVED BY RAYLEIGH LIDAR 1. CASE STUDIES

R. Wilson, M. L. Chanin, and A. Hauchecorne

Service D'Aéronomie du CNRS, Verrieres le Buisson, France

Abstract. Density and temperature mesoscale fluctuations as observed in the stratosphere and mesosphere by means of two Rayleigh lidars with high resolution in time (15 min) and space (300 m), have been analyzed in some particular cases corresponding to different seasonal conditions. These case studies are characteristic of recurrently observed patterns and thus provide a description of the mesoscale fluctuation field in the middle atmosphere. The spatial, temporal, and spectral characteristics of the fluctuations are described and discussed in the framework of the gravity wave interpretation. Dominant wave modes with large period and large vertical wavelength (inertia-gravity waves) are frequently observed in the stratosphere and lower mesosphere. These low-frequency modes are not generally observed above 50- to 55-km altitude, suggesting a strong damping of such waves in the mesosphere. The vertical growth of potential energy density indicates that the wave motions are generally not conservative in the middle atmosphere. The gravity waves amplitude appears too small to produce convective instabilities in the stratosphere. On the contrary, the amplitude of the fluctuations is close to the convective saturation limit deduced from the linear theory for wavelengths up to 3-5 km in the lower mesosphere, and up to 6-8 km above 60 km altitude. Furthermore, convectively instable layers, which can persist for periods longer than 1 hour, have been frequently observed in the mesosphere.

1. Introduction

It now appears firmly established that gravity waves play a major role in the momentum and thermal budget of the mesosphere [Lindzen, 1981; Holton, 1982; Fritts, 1984; Garcia and Solomon, 1985]. Dissipation processes, which induce a convergence of the vertical fluxes of horizontal momentum and energy, lead to an acceleration of the mean flow, and to the production of turbulence. The momentum convergence due to wave dissipation induces the reversal of the vertical mean wind gradient, thus a meridional flow and therefore the mesospheric temperature distribution known to be far from radiative equilibrium [Murgatroyd and Singleton, 1961]. More recently, it has been suggested that gravity waves also play an important role in the momentum budget of the stratosphere [Miyahara et al., 1986, Palmer et al., 1986].

The mean flow acceleration and turbulent diffusion induced by the wave saturation have been first parameterized by Lindzen [1981] in the framework of the linear theory of gravity wave. The wave saturation refers to those processes limiting the amplitude of the waves due to instabilities arising from the large amplitude of the fluctuations (for a review see Fritts [1984] and Fritts and Rastogi [1985]). Despite the success encountered by the linear theory, the involved scheme of the wave-mean flow interaction appears to be relatively simple and requires important theoretical and observational efforts in order to be better understood and parameterized. Numerous questions remain: what are the typical energy levels of the gravity wave field in the stratosphere and mesosphere? What is the vertical energy growth rate of the waves? Is there a significant seasonal or geographical variability of the wave activity? What are the dominant dissipative processes: convective or dynamical instabilities or other processes This paper will bring elements of answers for some of these issues.

Up to the present, most of the mesoscale fluctuations data in the middle atmosphere have been obtained by using radar techniques, rockets sounding, or balloon-borne instruments. The horizontal and vertical wind fluctuations are observed by radar both in the troposphere and lower stratosphere [Balsley and Garello, 1985; Fritts et al., 1988] and in the upper mesosphere [Vincent, 1984; Meek et al., 1985; Vincent and Fritts, 1987] but radars are blind in part of the middle atmosphere. Rocket data, on the other hand, have allowed the study of wind and temperature fluctuations in the 20- to 65-km altitude range from a large number of rocket ranges [Hirota, 1984; Hirota and Niki, 1985; Hass and Meyer, 1987], but the data are obtained in a sporadic manner. Balloon borne instruments give access to the fine structure of the fluctuation field [Barat, 1982; Cot and Barat, 1986], the altitude range being limited to about 25 km. Rayleigh lidar offers the unique feature of high resolution routine measurements of the density or temperature fluctuations, in the 30- to 75-km altitude range, where radars and in situ measurements are not possible and rocket soundings sporadic. The use of lidar in this height range thus complements to the other techniques and has now proved to be quite powerful to measure the mesoscale fluctuations in the middle atmosphere. Preliminary results were reported during the early phase of the development of this technique [Chanin and Hauchecorne, 1981, 1984; Shibata et al., 1986,

Paper number 90JD02231.
0148-0227/91/90JD-02231$05.00

1988] and from a relatively low performance system [Gardner et al., 1989]. The purpose of this paper is to describe and to discuss the main features of the mesoscale fluctuation field from observations obtained by two performing Rayleigh lidars. The fluctuations are interpreted in the framework of the gravity wave theory. Case studies, characteristic of recurrently observed wave patterns, are analyzed, thus providing a description of the wave field in the stratosphere and mesosphere. A climatological study, performed over a large data set, is reported in a separate paper.

This paper is organized as follows. In the second section the data base and the relevant parameters are described. The different data processing methods, giving access to various wave features, are reviewed in section 3. From typical particular cases the main characteristics of the gravity wave field in the middle atmosphere are described in section 4: dominant modes, vertical anisotropy of the wave field, spectral energy density versus vertical wave number, vertical growth of energy density per unit mass. The frequent occurrence of unstable lapse rate in the mesosphere is also shown. The results and conclusions are summarized in section 5.

2. The Data Base

The backscattered light from a pulsed laser beam sent vertically into the atmosphere, provided that Mie scattering could be neglected (i.e., above 30 km) and in the absence of any resonant line, is due to Rayleigh scattering from neutral molecules and is thus proportional to the atmospheric density. The uncertainty on the density measurement is simply related to the number of received photons, n(z), and depends upon the spatial and temporal integration of the lidar signal. The statistic of received photons being a Gaussian function (asymptotic limit of a Poisson distribution) the standard deviation of the density measurement is simply proportional to $n(z)^{-1/2}$.

As described in earlier publications [Hauchecorne and Chanin, 1980; Chanin and Hauchecorne, 1984], the absolute temperature profile can be deduced from the relative density measurements by assuming the hydrostatic equilibrium, applying the ideal gas law and fitting the temperature profile with an atmospheric model (Cospar International Reference Atmosphere (CIRA), 1986) at the upper altitude of the measurement. This upper limit altitude, z_{sup}, is defined as the height where the relative statistical error on the density reaches 15%, typically about 80 to 85 km for a temporal integration of 15 min. The temperature T(zi) in a layer of thickness Δz centered on the altitude z_i is given by

$$T(z_i) = \frac{g_i \Delta z}{R \, \mathrm{Ln}\left(1 + \rho_i g_i \Delta z / \left(P(z_{sup}) + \sum_{z=z_i}^{z_{sup}} \rho_z g_z \Delta z \right)\right)} \quad (1)$$

where ρ_i and g_i are respectively the density and the Earth acceleration at altitude z_i, R the air constant and $P(z_{sup})$ the pressure estimated at height z_{sup} from the CIRA 1986 model.

There are now two operating lidar stations in the south of France, located in two sites different with respect to orography: the Observatoire de Haute Provence (OHP) in the foothills of the Alps (44°N, 6°E) and the Centre d'Essais des Landes at Biscarosse (BIS) on the Atlantic Coast (44°N, 1°W). Routine measurements have been performed on clear nights since June 1981 at OHP and since March 1986 at BIS. High spatial and temporal resolution data allow the study of gravity wave motions with 300 m vertical integration and 15 min integration time. A very large data base has been acquired: it consists of about 100 nights a year, each night duration lasting between 3 and 14 hours, i.e. more than 10,000 vertical density profiles, in an altitude range which has been thus far barely explored.

Only a part of these nights, about 100, have been individually studied in great details. From this limited but already large number of case studies, it appears that some wave patterns are very frequently observed. The few cases presented here are characteristic of recurrent observations and thus provide a meaningful description of the gravity wave field in the middle atmosphere. These particular cases have been selected either because measurements were obtained simultaneously at both sites (May 29, 1986; December 17, 1987) or because they correspond to long measurement periods (August 7, 1985 at OHP, January 28, 1989 at BIS). In a single case, on May 29 at BIS, wind measurements from tracked rocketsondes were obtained simultaneously with the temperature measurements from Rayleigh lidar.

Let us briefly describe the parameters of interest for wave studies which are made available by Rayleigh lidar. It should be first recalled that, with regards to gravity wave motions, it is equivalent to consider the density or the temperature relative fluctuations (the pressure perturbations being negligible) provided that the vertical scales of the fluctuations are not much larger than the atmospheric density scale height, $H\rho$. The relative density fluctuations, ρ'/ρ_o, are estimated as the first order perturbation term of the vertical profile of $\log(\rho)$. The relative perturbations of density (ρ'/ρ_o) or temperature (T'/T_o) are extracted by subtracting from the raw vertical profile (or from its logarithm) a smoothed profile or a third-order polynomial fit. The smoothed profile is obtained by applying a finite impulse response filter, symmetric and nonrecursive, the so-called discrete prolate spheroidal filter (DPSF) [Mathews et al., 1983]. Examples of temperature vertical profiles, resulting from 15-min integration time and 1-km vertical resolution, are given in Figure 1. The shaded area correspond to plus or minus 1 standard deviation. The relative uncertainty for such spatial and temporal resolution, which could vary from one night to another depending upon the laser power and upon the atmospheric transmission, is typically around 0.2% at 30 km, 1% at 55 km, and 5% at 70 km. Vertical profiles of relative temperature perturbations corresponding to the temperature profiles shown in Figure 1 are plotted in Figure 2.

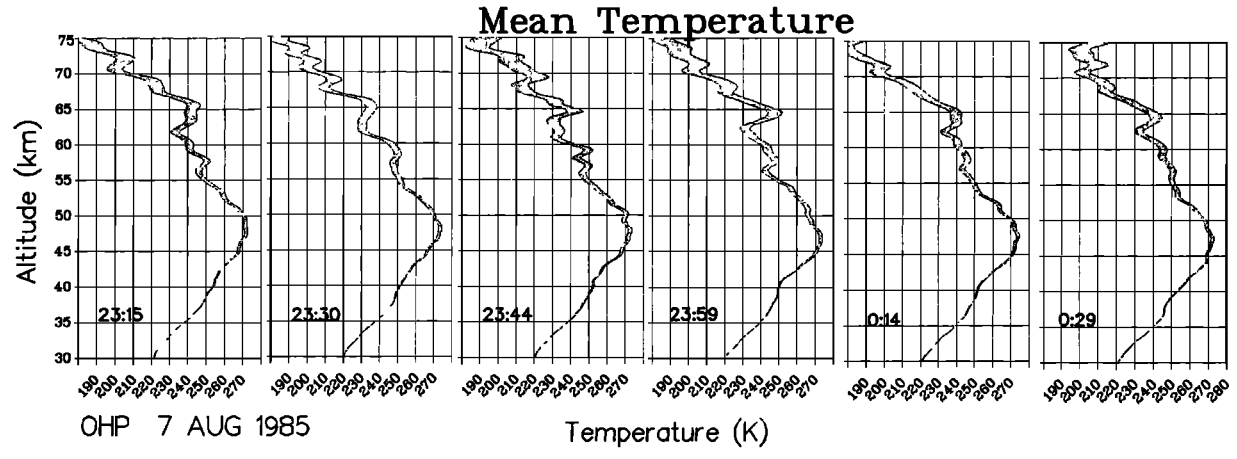

Fig. 1. Temperature profiles obtained by Rayleigh lidar on August 7, 1985, at OHP. The temporal resolution is 15 min, the vertical resolution is 1 km.

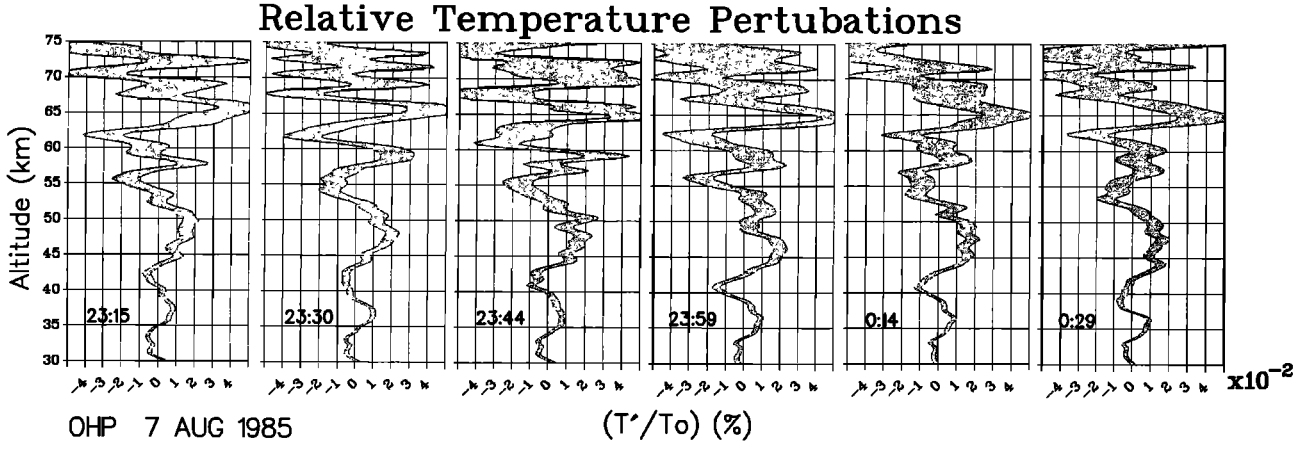

Fig. 2. Relative fluctuations of temperature corresponding to the temperature profiles shown in Figure 1. The perturbations are extracted by removing a smoothed profile (DPS filter, cutoff wave number 1/12000 m^{-1})

From the mean density or temperature profiles deduced from a low-pass filtering of the data, the static stability characterized by the local Brunt-Väisälä frequency, N(z), is given by

$$N^2(z) = -g\left(\frac{1}{\rho_o}\frac{\partial \rho}{\partial z} - \frac{g}{c_s^2}\right) = \frac{g}{T_o}\left(\frac{\partial T_o}{\partial z} + \frac{g}{C_p}\right) \qquad (2)$$

where g is the Earth acceleration, c_s the sound velocity, C_p the air specific heat at constant pressure, and z the vertical coordinate.

Density or temperature fluctuations are associated with vertical displacement of the atmospheric fluid and therefore are related to the available potential energy of the fluctuations. Indeed, for a vertical displacement relative to an equilibrium position, ξ, the potential energy per unit mass, Ep, is given by

$$Ep = \frac{1}{2}N^2\langle\xi^2\rangle = \frac{1}{2}\left(\frac{g}{N}\right)^2\left\langle\left(\frac{\rho'}{\rho_o}\right)^2\right\rangle \equiv \frac{1}{2}\left(\frac{g}{N}\right)^2\left\langle\left(\frac{T'}{T_o}\right)^2\right\rangle \qquad (3)$$

where brackets indicate a spatial or temporal average.

The temporal characteristics of the temperature (or density) fluctuations are obtained from the successive vertical profiles of the perturbations which give the apparent frequency of the wave, σ. Indeed, it is not possible to directly estimate from ground based measurements the intrinsic frequency, $\omega(z)$, in the reference frame of the mean flow, as it depends upon the mean wind velocity, $\mathbf{u}(z)$, the horizontal wave number $\mathbf{k_h}$, and the relative direction of propagation of the wave with respect to the mean flow:

$$\omega(z) = \sigma - \mathbf{k_h} \cdot \mathbf{u}(z) \qquad (4)$$

3. Data Processing

The distribution of gravity wave energy as a function of altitude, time, vertical wave number, and (apparent) frequency is described by means of various data processing

methods which are being presented here. Each of these methods gives access to different wave parameters in several altitude and spectral ranges. The gross features of the wave field, i.e., the vertical and temporal scales of the dominant wave modes, are viewed by time-height perturbation plots. The spectral energy distribution is given by the vertical and frequency spectra, whereas the spatial (vertical) energy distribution is estimated by a complex demodulation of the perturbation profiles in several wavelength bands. For each of these methods, the definition of the perturbation terms will be slightly different as described below.

From dimensional arguments, it has been shown by Dewan and Good [1986] that the power spectral density (PSD) of the relative density (or temperature) fluctuations of a saturated gravity wave field is proportional to $N^4/(g^2m^3)$. The perturbed densities are thus normalized as $(g/N^2)(\rho'/\rho_o)$ in order to provide a comparison between the vertical spectra obtained in various locations, times, and height ranges, with respect to the saturation limit. In order to reduce edge effects a Welch window is applied to the spatial series. The power spectrum, estimated by a simple Fourier transform, is then normalized to the raw variance. The daily mean spectrum is averaged upon the individual spectra (resulting from 15-min integrated profiles) obtained for a given day. It has been verified that the noise of the lidar signal due to the uncertainty on the photon counting has a white spectral response. The white noise level is evaluated in the high wave number portion of the mean PSD (where the signal-to-noise ratio is low), that is to say, for wavelengths smaller than 1 km and is subtracted from the raw spectrum. The uncertainty on the raw power spectrum, estimated in the standard way, is proportional to the estimated PSD. However, because of the variable signal-to-noise ratio versus wave number (the noise being subtracted), the uncertainty on the resulting power spectrum should be proportional to the signal-to-noise ratio. The relative uncertainty on the resulting PSD is thus assumed to be of the form

$$\frac{\Delta(S(k)-B)}{S(k)-B} = \frac{1}{n_s^{1/2}} \frac{S(k)}{S(k)-B} \qquad (5)$$

where S(k) is the power spectral density of the raw data, B the white noise level, and n_s the number of spectra over which the average is performed.

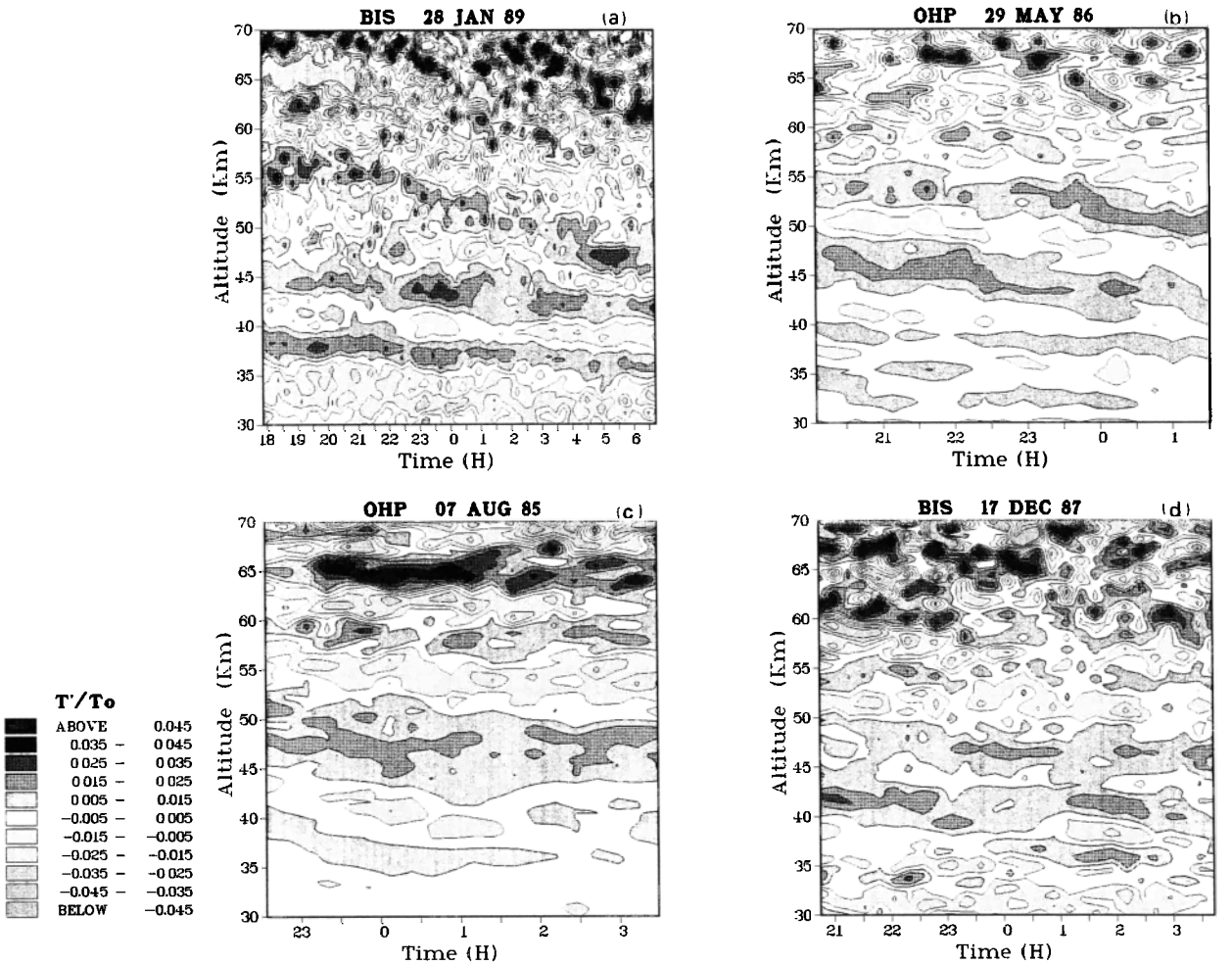

Fig. 3. Time-height contours of temperature relative perturbations, on (a) January 28, 1989, at BIS; (b) May 29, 1986, at OHP; (c) August 7, 1985, at OHP; and (d) December 17, 1987, at BIS.

Spectral analysis as a function of vertical wave number is performed in three altitude ranges: the upper stratosphere (30 to 45 km), the lower mesosphere (45 to 60 km), and the 55- to 70-km height range. The potential energy density per unit mass is estimated by integrating the PSD over vertical wave numbers between 1/15 and 1/0.6 km^{-1}, subtracting the noise variance and scaling by the averaged value of N^2.

The time evolution of the density fluctuations are described by a two dimensional (2D) spectral analysis as a function of vertical wave number and (apparent) frequency. A frequency Fourier transform is applied upon the successive vertical wave number spectra giving a qualitative insight into the temporal characteristics of the fluctuations. The 2D spectrum shows, for each wave number, the phase evolution of the successive Fourier Transforms of the density perturbations profiles. The zero frequency term represents the power spectrum of the fluctuations with periods longer than the measurement duration, such fluctuations being vertically resolved. The integration of the 2D spectrum over frequencies gives of course the power spectrum versus vertical wave number. According to the relative sign of the frequency and wave number terms of the phase, expressed as $\exp(mz \pm \omega t)$, the upward and downward vertical phase velocities can be identified. Provided that $\omega << N$ (as it is the case in this study), the dispersion relation of a monochromatic gravity wave is

$$\omega^2 = f^2 + N^2 \frac{k_h^2}{m^2} \tag{6}$$

where f is the inertial frequency, k_h and m being the horizontal and vertical wave numbers, respectively. The vertical group velocity, C_g, is thus

$$C_g = \frac{\partial \omega}{\partial m} = -\frac{\omega}{m}\left(1 - \frac{f^2}{\omega^2}\right) \tag{7}$$

The vertical group velocity, C_g, and the vertical phase velocity, C_z ($=\omega/m$), are thus in opposite direction. Therefore the energy flux of a wave the vertical phase velocity of which propagates downward is directed upward. Even though the result could be biased, owing to the frequency Doppler shift, an observed recurrent behavior would be a clear indication of a vertical asymmetry of the wave field.

A complex demodulation of the density profiles is also performed in three wavelength bands centered at 6, 5, and 4 km. The purpose of the complex demodulation is to estimate the variation of the variance versus altitude in a given wave number band of the wave spectrum. The spatial series is multiplied by $\exp(-im_c)$ before applying a low-pass filter (DPSF), therefore providing the variance of the fluctuations in a spectral band centered on m_c. The spectral width is a function of the cutoff wave number of the filter. The used DPS filter has a cutoff wave number at 1/10 Km^{-1}. An average of the variance over the three neighboring spectral intervals (partially overlapping) will be presented, taking into account the fact that the vertical scales of the waves could change significantly in the height range under study. For the demodulation analysis the perturbation term is defined as $(g/N)(\rho'/\rho_o)$, the variance of which is twice the available potential energy. As for the spectral analysis, the noise level is estimated by estimating the mean variance of short scale fluctuations, smaller than 1 km, and is removed from the raw variance. The uncertainty on the resulting variance is evaluated in the same way as for the spectral analysis (equation (5)).

The spectral and demodulation analyses are performed from density profiles which are simply proportional to the lidar signal (i.e., the number of backscattered photons), whereas temperature profiles result from a differentiation of the density profiles. Indeed, the white noise level is better defined from the density data, because it could be biased from the temperature data owing to the differentiation and to the initial assumption on the pressure at the top of the profile. In any case, whether temperature or density fluctuations are used for such analyses the results are not significantly different, provided that they are obtained far enough from the top of the profile, as is the case in this study.

4. Gravity Wave Characteristics

The main features of the gravity wave field in the stratosphere and mesosphere, as observed by two Rayleigh lidars at mid-latitude, are now described from a few selected cases, characteristic of recurrently observed wave patterns. The presence of dominant low-frequency wave modes in the stratosphere, the potential energy distribution versus vertical wave number, apparent frequency and altitude, and finally the frequent occurrence of convectively instable layers in the mesosphere will be shown.

4.1. A Dominant Gravity Wave Mode in the Stratosphere

Most often, a dominant oscillatory mode is observed in the stratosphere and lower mesosphere. This dominant mode has a large apparent period ranging typically from 6 hours to infinity, a downward phase velocity, and a large vertical wavelength, from 5 to 10 km. Examples of time-height contours of relative temperature perturbations are shown in Figure 3. These data have been obtained during different seasons and thus in various mean flow conditions: January 28, 1989, at BIS; August 7, 1985, at OHP; May 29, 1986, and December 17, 1987, at both sites. From these four examples, which illustrate a recurrent pattern, a dominant oscillation of several kilometers' vertical wavelength and several hours' period can be clearly identified. Except on August 7 (Figure 3c), this low-frequency mode seems to disorganize and to disappear in the lower mesosphere, above 55 or 60 km altitude. The temperature perturbation plot, shown in Figure 3d, for the measurements of December 17, 1987, at BIS, exhibits a somewhat more complex pattern which probably results from the superposition of several large amplitude oscillatory modes.

In a single case, on May 29, 1986, at Biscarosse, wind measurements, obtained from tracked rocketsonde, were

collected on the site simultaneously with the lidar measurements. The time-height plot of the temperature fluctuations as well as the horizontal wind perturbation profile (Figure 4) shows the presence of a dominant oscillatory mode in the stratosphere and lower mesosphere between 35- and 55-km altitude with 6- to 12-km wavelength and roughly 10 hours' period. The zonal and meridional wind components have a roughly constant phase lag up to 55 km altitude. Above this height the pattern is somewhat more complicated, resulting probably from wave superposition. In this single opportunity it has been possible to clearly identify a gravity wave from the polarization relationships, i.e., the relationships between the different perturbed variables. From the WKB solutions of the linearized perturbations equations, the horizontal wind fluctuations in the direction toward which the wave is travelling, U', and in the perpendicular direction, V', and the temperature relative fluctuations, T'/T_o, of a monochromatic gravity wave are related as follows:

$$V' = -i\frac{f}{\omega}U' = -\left(\frac{1-\omega^2/N^2}{\omega^2/f^2-1}\right)^{1/2}\frac{g}{N}\left(\frac{T'}{T}\right) \qquad (8a)$$

$$U' = -i\left(\frac{1-\omega^2/N^2}{1-f^2/\omega^2}\right)^{1/2}\frac{g}{N}\left(\frac{T'}{T_o}\right) \qquad (8b)$$

where $i=\sqrt{-1}$, the other notations being defined as previously. The inertial frequency, f, is close to $2\pi/17$ hours^{-1} at 44°N. The wind perturbations perpendicular to the direction of the wave propagation, V', is 180° out of phase with the temperature fluctuations and in quadrature with U' (equation (8a)), U' and T' being of course in quadrature (equation (8b)). The ratio, U'/V', is proportional to the intrinsic frequency, ω. Therefore the amplitudes of the temperature and wind perturbations are also related to ω. The direction of the wave propagation is estimated, assuming a quasi-monochromatic wave, by determining analytically the major axis orientation of the wind elliptical hodograph [Kundu, 1976; Cot and Barat, 1986]. The direction towards which the wave propagates is found to be close to −0.8 rad (anticlockwise from east). The propagation direction of the wave with respect to the mean flow (directed towards west-south West) make an angle of roughly π/3 (anticlockwise).

Figure 5 shows the horizontal wind fluctuations projected in the direction of the wave propagation and in the perpendicular direction just as the normalized temperature perturbations $(g/N)(T'/T_o)$ between 33- and 50-km altitude. The fluctuations are extracted by a band pass filtering (cutoff wavelengths at 3 and 12 km) of the vertical profiles. The phase relationships between the two horizontal wind components are consistent with the polarization relations (equation (8a)). The temperature fluctuations are about 180° out of phase with V' between 33 and 50 km (equation (8b)). Below and above these heights the phase relationship between the temperature and wind fluctuations do not seem consistent with the polarization relationships (equation (8a), (8b)), suggesting a superposition of other wave modes. An inertia-gravity wave is thus clearly identified over about two vertical wavelengths, even though other wave modes are probably superimposed. The main characteristics of this inertio-gravity wave, as deduced from the wind and temperature measurements over two vertical wavelengths, are summarized in Table 1. The horizontal wind hodograph (Figure 6) shows a clockwise rotation of the wind vector with altitude (thus an upward energy flux). The ratio f/ω,

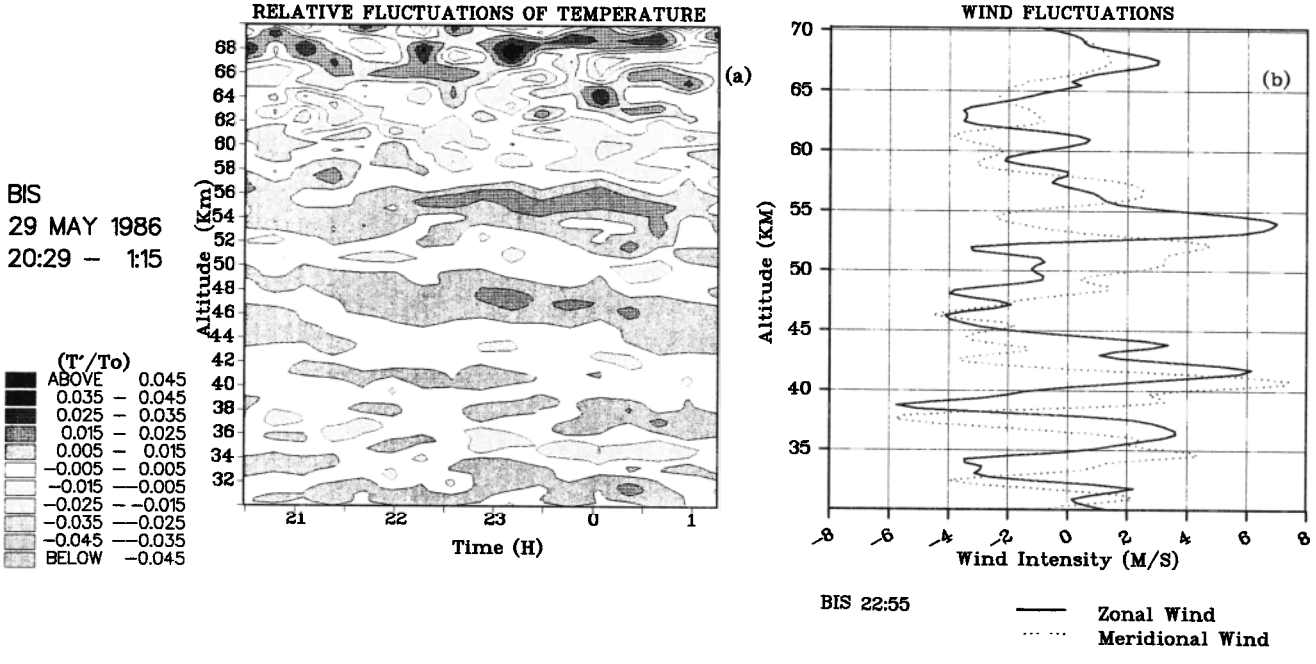

Fig. 4. Time-height contours of (a) the temperature relative fluctuations observed by Rayleigh lidar and (b) the horizontal wind fluctuations obtained from tracked rocketsonde on May 29, 1986, at BIS.

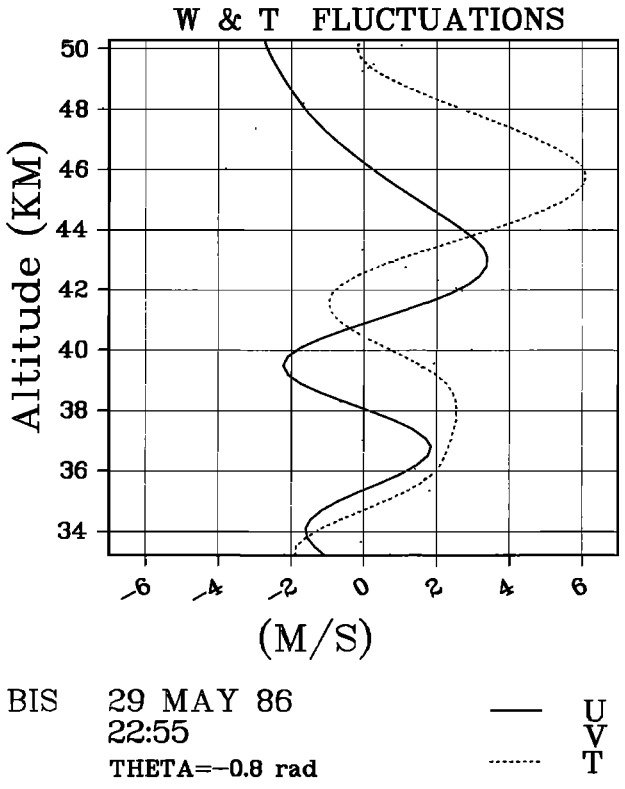

Fig. 5. Vertical profiles of the horizontal wind fluctuations (projected in the direction of the wave propagation and in the perpendicular direction) and normalized temperature fluctuations $(g/N)(T'/T_0)$ obtained with a band pass filter centered on 6 km between 33- and 50-km altitude.

close to 0.75, indicates an intrinsic period of the order of 13 hours. The horizontal wavelength, deduced from the dispersion relationship (equation (6)), should be therefore close to 1500-2000 km. The vertical phase velocity, as observed from the temperature fluctuations (Figure 4), is directed downwards (roughly -0.2 to -0.4 m s^{-1}), as expected for a wave with a positive intrinsic horizontal phase velocity (equation (7)). Note also that the wave pattern observed the same day at OHP (Figure 3b), 550 km east of BIS, is quite similar above 40 km altitude : it shows a vertical wavelength of 6 to 8 km and a downward phase velocity of about -0.3 m s^{-1}.

The vertical component of the perturbation velocity, w', as well as the meridional component, v', are related to the zonal wind component [Gossard and Hooke, 1975] by

$$w' = -\frac{k_h^2}{m}\left(\frac{1}{1 + ia\cdot tg(\tau)}\right) u' \qquad (9a)$$

$$v' = -\left(\frac{ia - tg(\tau)}{1 + ia\cdot tg(\tau)}\right) u' \qquad (9b)$$

where τ is the angle defining the direction of the wave propagation (anticlockwise from east), $tg(\tau)=l/k$, l and k being the meridional and zonal wave number respectively, and $a=f/\omega$. Following the method described by Eckermann and Vincent [1989], the vertical fluxes of the zonal and meridional horizontal momentum ($\langle u'w'\rangle$ and $\langle v'w'\rangle$, respectively) are written

$$\langle u'w'\rangle = -\frac{k_h}{m}\frac{\langle u'v'\rangle}{\sin\tau(1-a^2)} \qquad (10a)$$

Table 1. The Inertia-Gravity Wave Characteristics Observed on May 29, 1986, at BIS

	From 33 to 39 km	From 39 to 49 km
Polarization f/ω	0.78	0.73
Direction from east, rad	-0.82	-0.75
Vertical wavelength, km	6	10
Horizontal wavelength, km	1640	2208
Momentum flux, N m^{-2}		
$\rho_0\langle u'w'\rangle$	2.47×10^{-5}	0.67×10^{-5}
$\rho_0\langle v'w'\rangle$	-2.17×10^{-5}	-0.63×10^{-5}
Induced acceleration, m s^{-1} d^{-1}		
$-1/\rho o\Delta/\Delta z(\rho_0\langle u'w'\rangle)$	4.1×10^{-2}	
$-1/\rho o\Delta/\Delta z(\rho_0\langle v'w'\rangle)$	-3.6×10^{-2}	
Vertical group velocity, m s^{-1}	0.49×10^{-1}	1.02×10^{-1}
Horizontal group velocity, m s^{-1}	34.8	50.0
Kinetic energy density, j kg^{-1}	4.2	12.1
Potential energy density, j kg^{-1}	1.9	5.6
Total energy density, j kg^{-1}	6.1	17.7
Vertical energy flux, j m^{-2} s^{-1}	2.18×10^{-3}	4.26×10^{-3}
Horizontal energy flux, j m^{-2} s^{-1}	1.55	2.1

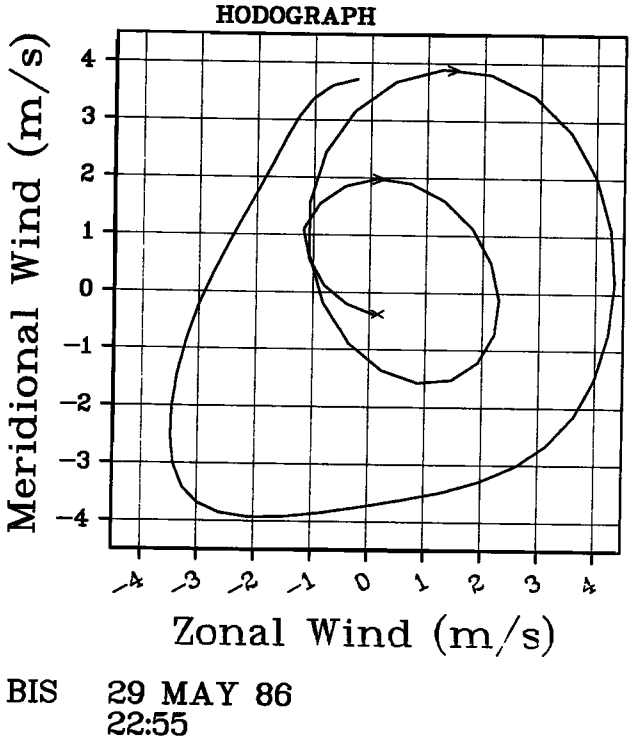

Fig. 6. Hodograph of the horizontal wind fluctuations between 33- (indicated by x) and 50-km altitude. The wind vector is turning clockwise.

$$\langle v'w' \rangle = - \frac{k_h}{m} \frac{\langle u'v' \rangle}{\cos\tau(1-a^2)} \qquad (10b)$$

the brackets denoting here a vertical average. On inserting in these relations the inferred values for f/ω, k_h/m, $\langle u'v' \rangle$, and τ, and the atmospheric density ρ_o (CIRA, 1986), the mean values for $\rho_o\langle u'w' \rangle$ and $\rho_o\langle v'w' \rangle$ can be estimated [Eckermann and Vincent, 1989]. The wave-induced acceleration between 33- and 50-km altitude have been evaluated from these momentum fluxes estimations. These values are reported in Table 1. Even though very small, the order of magnitude of the induced acceleration was found to be nearly the same in the zonal and meridional direction. The wave-induced acceleration is in a direction opposite to the zonal component of the mean flow (eastward) and in the same direction than the (weak) meridional component of the mean flow (southward).

4.2. The Vertical Anisotropy of the Wave Field

From most of the case studies performed, the observed inertia-gravity waves exhibit a downward vertical phase velocity of the order of a few tens of centimenters per second. Four examples of two-dimensional spectra, function of vertical wave number, m, and apparent frequency, σ, resulting from density measurements in the upper stratosphere (30-45 km), are shown in Figure 7. The

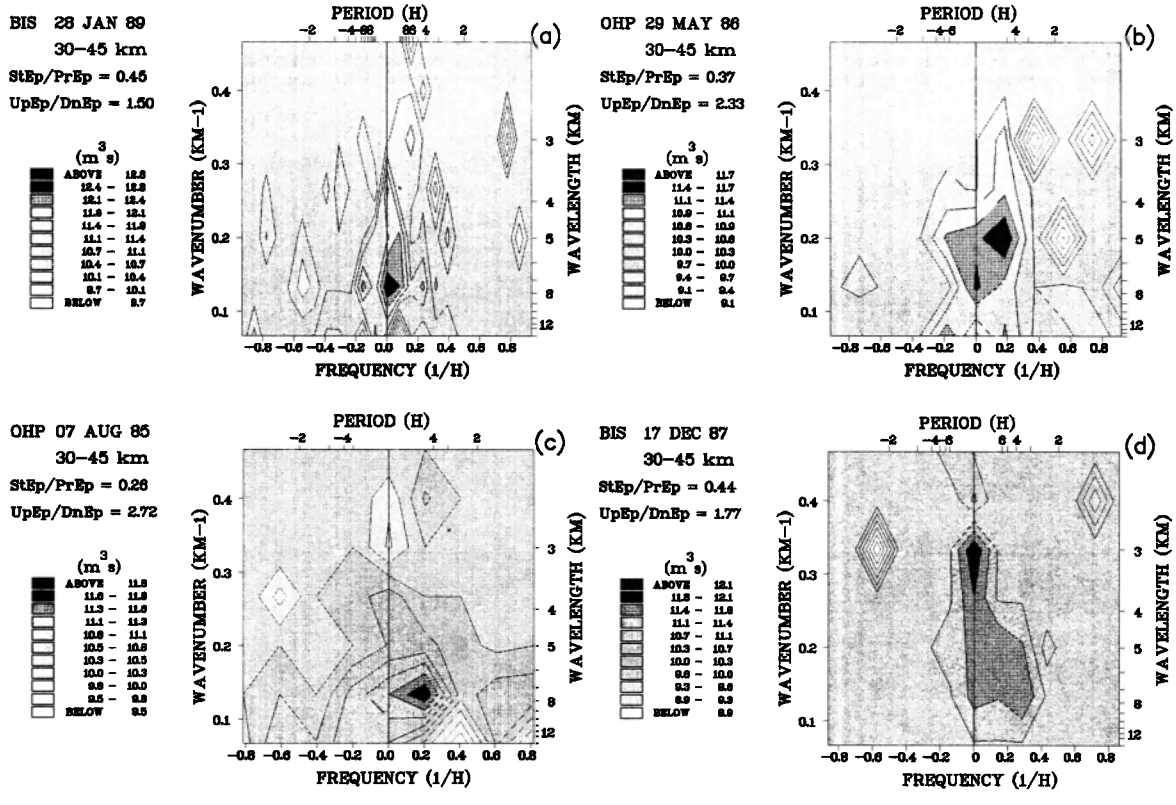

Fig. 7. Two dimensional spectra, function of the vertical wave number and apparent frequency, of the density fluctuations in the stratosphere (30-45 km). The ratios of upward to downward propagating energy (UpEp/DnEp) and of stationary to propagating energy (StEp/PrEp) are indicated. (a) BIS, January 28, 1989; (b) OHP, May 29, 1986; (c) OHP, August 7, 1985; (d) BIS, December 17, 1987.

dominant low-frequency and low wave number wave modes are easily identified from each of these examples. On December 17, a low-frequency mode with a relatively small vertical wavelength (3 km) is observed whereas for the other cases the vertical wavelength of the dominant mode ranges between 5 and 8 km. The frequency term of the phase (expressed as $\exp(mz \pm \sigma t)$ with $\sigma>0$) of this dominant wave modes is generally positive. It implies a downward vertical phase velocity, indicative of an upward energy flux. The energy ratio of the fluctuations with upwards and downwards vertical phase velocity respectively is reported in Figure (7). This ratio ranges between 1.5 and 2.7. The PSDs of the fluctuations with vertical phase velocities propagating upward and downward (resulting from an integration over the positive and negative frequencies, respectively) are shown in Figure 8. A vertical asymmetry of the wave field is observed, 65 to 80 % of the energy content of the progressive waves (i.e., resolved frequencies) having downward vertical phase velocity.

The two-dimensional spectra resulting from density measurements in the mesosphere, from 55 to 70 km (Figure 9), show that the dominant wave modes have somewhat higher frequencies than at lower level. The energy ratio of the stationary waves (unresolved frequencies) to the progressive waves (resolved frequencies) decreases from about 0.3-0.4 in the stratosphere to 0.1 in the mesosphere. This frequently observed feature suggests that the waves should have relatively higher frequencies in the mesosphere than in the stratosphere.

It appears from most case studies that the vertical phase velocity of the dominant inertia-gravity waves observed in the upper stratosphere and lower mesosphere is very generally directed downward. Above 50- or 55-km altitude the lower-frequency waves frequently seem partially dissipated. A vertical asymmetry of the wave field (for vertical scales between 1 and 15 km) is generally observed, most part of the waves having downward vertical phase velocity indicating an upwards energy flux. Such a vertical asymmetry of the wave field has been observed in this height range from rocket soundings [Hirota and Niki, 1985, Eckermann and Vincent, 1989]. These findings are basically in agreement with the results shown above, suggesting that most part of the waves are generated below 30-km altitude, in the troposphere and lower stratosphere.

4.3. The Power Spectral Density

Before discussing the results concerning the density fluctuation PSDs, we first briefly recall some of the main results on the gravity wave saturation theory. Numerous

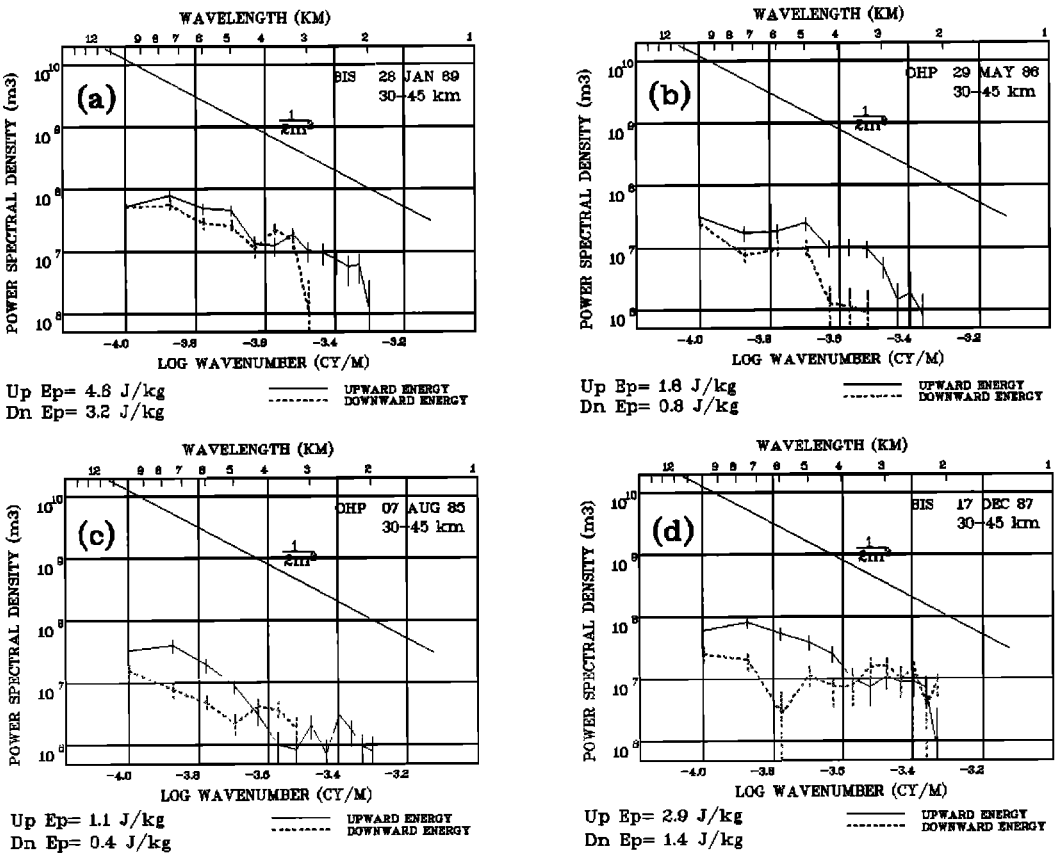

Fig. 8. The PSD versus vertical wave number of the fluctuations for which the vertical phase velocity propagates downward (i.e., upward energy flux) and upward (i.e. downward energy flux) obtained by integrating the 2D spectra over the positive and negative frequencies, respectively. (a) BIS, January 28, 1989; (b) OHP, May 29, 1986; (c) OHP, August 7, 1985; (d) BIS, December 17, 1987.

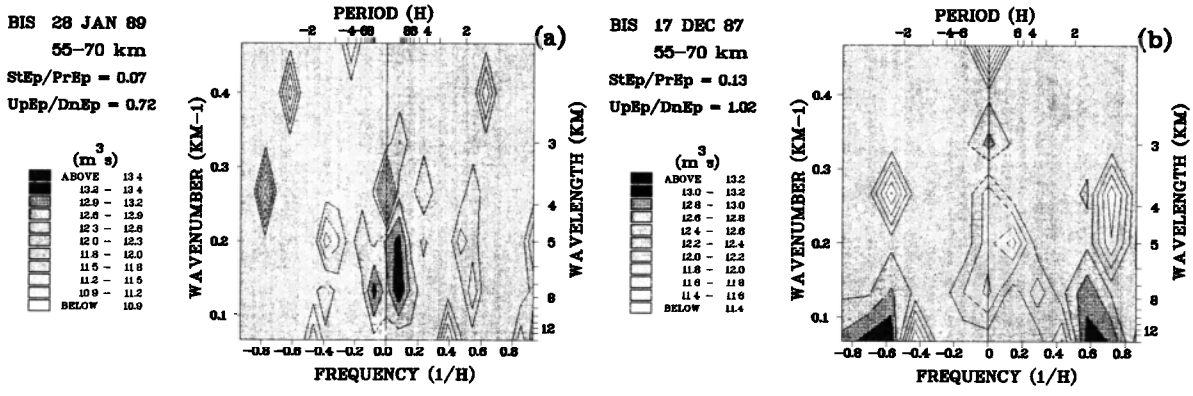

Fig. 9. Two dimensional spectra resulting from density measurements in the mesosphere (55-70 km) performed on (a) January 28, 1989, and (b) December 17, 1987, at BIS.

experimental evidences indicate a large similarity in both shape and amplitude of the mesoscale fluctuation PSDs as a function of wave number and frequency in the middle atmosphere [Dewan et al., 1984; Balsley and Garello, 1985; Nastrom and Gage, 1985; Smith et al., 1987; Hass and Meyer, 1987; Sidi et al., 1988; Fritts et al., 1988]. It has been suggested by Van Zandt [1982] that the observed mesoscale fluctuations spectra are due, as in the ocean [Garrett and Munk, 1975], to a random superposition of gravity waves, the so-called "universal spectrum." The shape and magnitude of the wind and temperature fluctuations PSDs versus vertical wave number are thought to be the consequence of

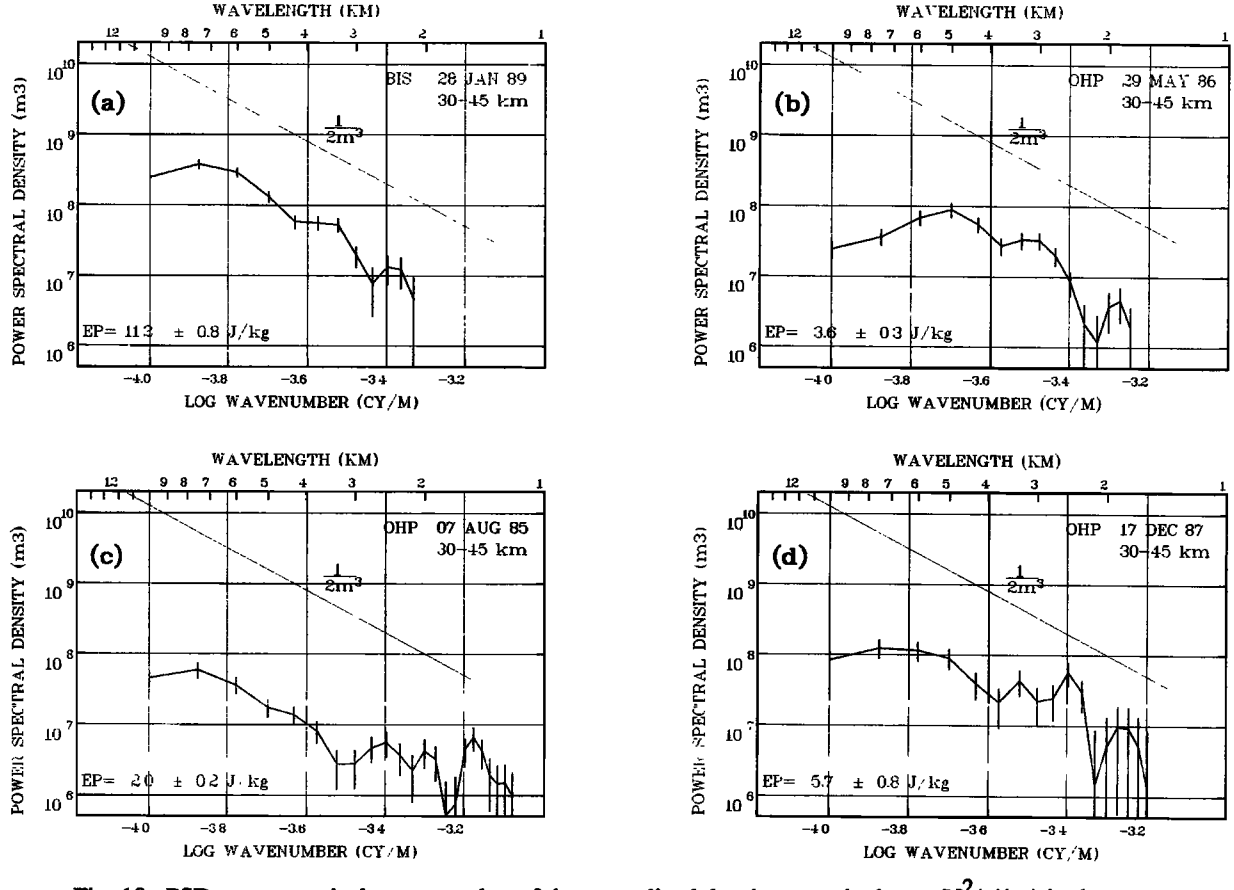

Fig. 10. PSD versus vertical wave number of the normalized density perturbations $g/N^2(\rho'/\rho_0)$ in the upper stratosphere (30-45 km). The spectra are plotted up to the larger wave numbers for which the signal-to-noise ratio is larger than unity. (a) BIS, January 28, 1989; (b) OHP, May 29, 1986; (c) OHP, August 7, 1985; (d) OHP, December 17, 1987.

the saturation processes [Dewan and Good, 1986]: the convective and/or dynamical instabilities induced by large amplitude waves acts to limit this amplitude to an upper value related to the vertical wave number. With these assumptions, the relative density (or temperature) fluctuations PSD versus vertical wave number of a saturated wave field is scaled as

$$F^{s}_{T'/T_o,\rho'/\rho_o}(m) \approx \alpha \frac{N^4}{g^2 m^3} \qquad (11)$$

where α is a proportionality factor ranging between 1/2 and 1/20, depending upon the spectral width of the saturated wave field [Dewan and Good, 1986; Smith et al., 1987, Sidi et al. 1988]. This estimate of the power spectra of saturated density fluctuations does not depend upon the frequency distribution of the waves owing to the assumption of convective instabilities as the only saturation mechanism.

PSDs versus vertical wave number of the normalized density fluctuations in the upper stratosphere (30-45 km) are shown in Figure 10. With the chosen normalization, the straight line $1/2m^3$ indicates the spectral limit (11) with α=1/2. An important variability in the spectral shape and magnitude is observed from a day to another in the accessible spectral domain. The density fluctuations PSDs in the upper stratosphere are 1 or 2 orders of magnitude less than the $1/2m^3$ limit for vertical wavelengths between 1 and 15 km ($1/200<\alpha<1/20$, i.e., much below the expected value for saturated waves). The standard deviation of the temperature fluctuations appears to be too small (between 1.5 and 2.5 °K) to produce convective instabilities in the upper stratosphere. Except on January 28, 1989, the power spectra are not scaled as m^{-3} in the low wave number part of the spectrum (i.e., for wavelength larger than 2-3 km). The spectral index (the power dependency of the spectrum versus vertical wave number) ranges between -2 and +1. The potential energy density per unit mass, estimated by integrating the PSD over wave numbers, varies within a factor of 6, ranging between 2 and 12 J kg^{-1}. It appears from these few examples that the potential energy density is larger during winter than during other seasons. This result will be confirmed from the statistical study.

The PSD of the normalized density fluctuations in the lower mesosphere (45 to 60 km) increases with altitude for all wave numbers (Figure 11a). The power spectra of the density fluctuations appear to be compatible with the spectral limit (11) for vertical wavelengths smaller than 3 or 4 km ($1/10<\alpha<1/4$). For larger vertical scale fluctuations the PSDs are much smaller than the saturation limit (11) ($\alpha<1/20$), the spectral index being also larger than -3. The standard

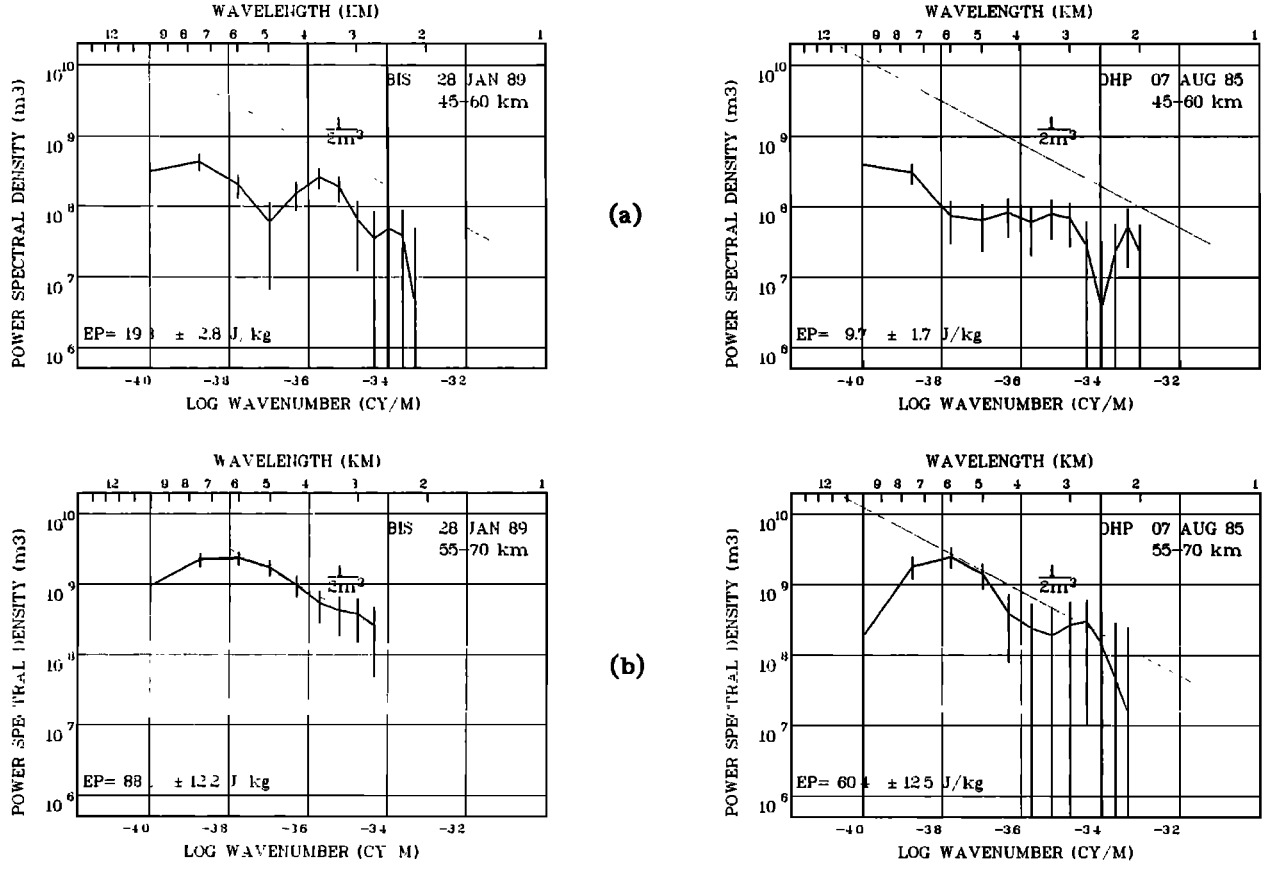

Fig. 11. PSD versus vertical wave number of the normalized density perturbation (a) in the lower mesosphere (45-60 km) and (b) in the middle mesosphere (55-70 km).

deviation of the temperature fluctuations is of the order of 2° to 3 °K, the potential energy density per unit mass increasing by a factor 2 to 5 from the upper stratosphere to the lower mesosphere. The fact that the density PSDs are not scaled as N^4 from the stratosphere to the mesosphere (as N^4 decreases by about a factor of 2 to 3) seems to indicate that the wave field is not convectively saturated (i.e., saturated through induced convective instabilities) in the stratosphere .

Normalized density fluctuations PSDs in the middle mesosphere (55 to 70 km), on January 28 and August 7, are shown in Figure 11b. At these heights, waves amplitude reach the saturation limit as defined in equation (11) ($\alpha \approx 1/2$) strongly suggesting that the wave field is convectively saturated above 60 km altitude for wavelengths up to 6 km. The spectral index seems to be consistent, within the error bars, with a -3 slope for wavelengths between 6 and 2-3 km. Furthermore, the standard deviation of the temperature fluctuations ranging between 3° and 5 °K, appears to be large enough to induce convective instabilities in an height range where the temperature gradient is negative.

The normalized density fluctuations PSDs, interpreted in the framework of the gravity wave saturation theory, thus indicate that the wave field is not convectively saturated in the upper stratosphere (30-45 km) within the accessible spectral domain (from 1- to 15-km vertical wavelength). As the altitude increases, the power spectral density increases for all wave numbers, reaching a spectral limit close to $N^4/2g^2m^3$ in the middle mesosphere. It strongly suggests that gravity waves reach saturation inducing convective instabilities for vertical wavelengths up to 6 km. A growth from the stratosphere to the mesosphere of a mean temperature PSD has also been observed by Shibata et al. [1988] from 13 Rayleigh lidar profiles. These findings seem to be in contradiction with those of Smith et al. [1987] and Tsuda et al. [1989], who have shown from in situ and MST radar measurements, that the horizontal wind PSDs are scaled by N^2 in the saturated range from the stratosphere to the mesosphere. This may indicate that dynamical instabilities (Kelvin-Helmoltz instabilities) are the main saturation processes in the stratosphere where low frequency waves appears dominant and where the amplitude of the density fluctuations seems to be small compared to any convective saturation limit. Nevertheless, no firm conclusions can be reached from the density measurements alone.

4.4. The Potential Energy Density Versus Altitude

The available potential energy density per unit mass (Figures 10 and 11) increases significantly from the upper stratosphere, where it is a few joules per kilogramme, to the middle mesosphere, where it reaches some 10 j kg^{-1}. The energy density per unit mass grows roughly by a factor 2 of to 4 over about two atmospheric scale heights (the exact values for the cases presented here are given in Figure 10 and 11). The vertical scale height of the energy density per unit mass, H_E ($=\Delta z/\ln\{Ep(z+\Delta z)/Ep(z)\}$), thus ranges between 10 and 20 km. Using the WKB solutions of the linearized perturbations equations, the potential energy density, Ep(z), of a conservative monochromatic gravity wave should be scaled as

$$Ep(z) \propto \frac{N}{|c-\overline{u(z)}|} \exp(z/H\rho) \qquad (12)$$

where z is the height, Hρ the density scale height, and $\overline{u(z)}$ the mean horizontal wind. Therefore a background wind shear can be the cause of large departure from an exponential growth particularly if the intrinsic phase speed of the wave, $c-\overline{u(z)}$, is small.

The potential energy densities versus altitude, as observed on January 28 and December 17 at BIS and on May 29 and August 7 at OHP, deduced by a complex demodulation of the signal averaged over three wavelength bands (centered on 6, 5 and 4 km), are plotted in Figure 12. The energy density is plotted up to the altitude where the signal-to-noise ratio is less than unity. The noise variance (dotted line in Figure 12), which is subtracted from the raw variance, increases with altitude as the density scale height. An increase of energy density is generally observed from the stratosphere to the mesosphere. However, the rate of energy growth varies considerably from one case to the other. In two cases (January 28 and December 17) the energy density is almost constant in the stratosphere whereas in another one (August 7) the growth is exponential with a scale height of the order of the density scale height. A minimum in the variance is observed in some cases above the stratopause level (January 28). This variance decrease could be due to the damping of the inertia-gravity waves often observed at that level (Figure 3a). An energy growth is quasi-systematically observed in the mesosphere at least up to 65 km. In a few cases, as on August 7, the energy scale height is close to the density scale height in the stratosphere and mesosphere.

From these selected case studies, on cannot clearly conclude about the energy density scale height as the energy growth is highly variable with altitude. This variability may be due to wind shears and/or dissipative processes. Nevertheless, the small energy growth frequently observed in the stratosphere seems to indicate that the waves are dissipated at these heights. Because the PSDs of the density fluctuations do not appear characteristic of a convectively saturated wave field (section 4.3), this suggest that the waves are dissipated through dynamical instabilities or any other processes. Conclusions on the vertical growth of the waves will be further achieved from the statistical study on a large number of cases.

4.5. Convective instabilities

The power spectra of the normalized density fluctuations and the inferred standard deviation of the temperature fluctuations both suggest that convective instabilities may occur in the mesosphere due to large waves amplitudes.

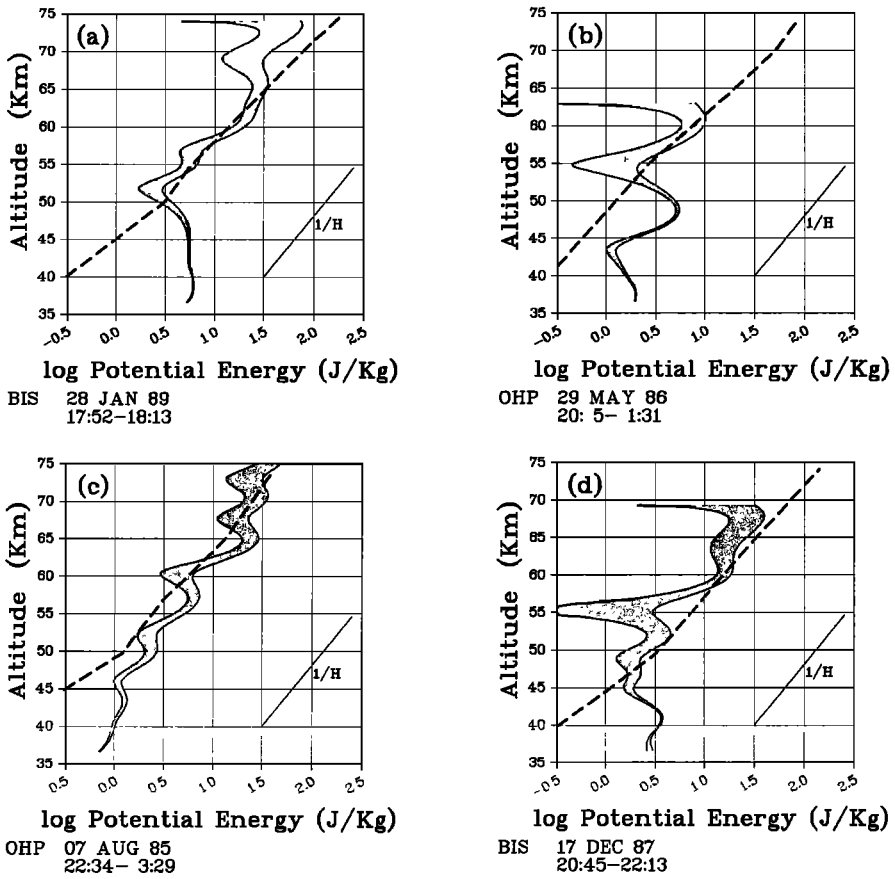

Fig. 12. Available potential energy density per unit mass versus altitude deduced by a complex demodulation of the signal averaged in three wavelength bands (centered on 6, 5, and 4 km). The noise level, deduced by demodulation on short scale fluctuations (smaller than 1 km) is plotted for comparison (dashed line). The variance of the fluctuations is plotted up to the altitude where the signal-to-noise ratio is larger than unity. (a) BIS, January 28, 1989; (b) OHP, May 29, 1986; (c) OHP, August 7, 1985; (d) BIS, December 17, 1987.

Vertical temperature profiles deduced from 1 hour integration time (in order to reduce the uncertainty), observed during the night of January 28, 1989; May 29, 1986; December 17, 1987, at BIS; and August 7, 1985, at OHP are plotted in Figure 13. Vertical gradients of temperature close to the adiabatic lapse rate (roughly $-10°$ km^{-1}) are observed in the mesosphere independently of the seasons, during winter (January 28, December 17), in summer (August 7), and in equinoctial conditions (i.e., in weak wind conditions as on May 29). These convectively unstable layers are observed either just above the stratopause level (May 29) or at higher levels. From comparing Figures 3 and 13, the unstable layers are frequently produced above the altitude where the dominant wave amplitude reaches a maximum (as on January 28, May 29 and August 7). Above this level, the dominant mode appears to be disorganized. Such instabilities seem thus clearly induced by the large amplitude of the waves. On January 28, just above the adiabatic lapse rate, a mesospheric temperature inversion occurs. Those are frequently observed in the mesosphere above large temperature gradient and are likely induced by gravity wave breaking [Hauchecorne et al., 1987; Hauchecorne and Maillard, 1990].

5. Conclusions

Density and temperature fluctuations, observed in the stratosphere and mesosphere by means of Rayleigh lidars with high spatial and temporal resolution (15 min and 300 m), have been analyzed in some particular cases in various seasonal conditions. These selected cases are characteristic of tipically observed wave patterns.

1. The presence of a dominant fluctuating mode of large period, typically 10 hours period, and large vertical wavelength, from 5 to 10 km, is very generally observed in the stratosphere and lower mesosphere. In a single case, when simultaneous wind and temperature measurements have been performed, an inertia-gravity wave has been clearly identified. The frequencies of the wave field seem to be relatively higher in the mesosphere than in the stratosphere, suggesting a strong damping of the lower-frequency waves in the lower mesosphere.

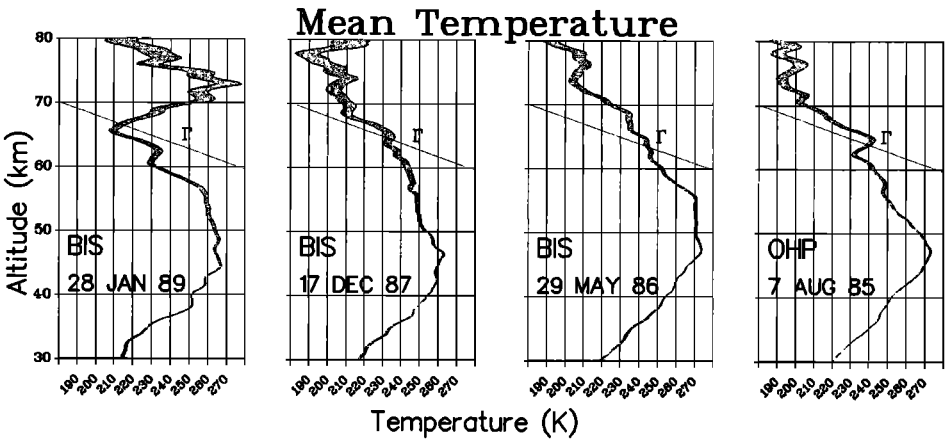

Fig. 13. Vertical temperature profiles, resulting from 1-hour integration time of the signal, observed on January 28, 1989; May 29, 1986; and December 17, 1987 at BIS and on August 7, 1985, at OHP.

2. The vertical scale height of the potential energy is most often larger than the density scale height, generally larger than 10 km. Nevertheless, in a few cases the energy scale height is close to the density scale height. The energy density growth is generally, but not systematically, smaller in the upper stratosphere and lower mesosphere, than above 55 km. Such a change in the energy scale height according to the altitude domain could be due partially to the mean wind reversal in the mesosphere.

3. If the gravity wave field does not appear to produce convective instabilities in the stratosphere, the amplitude of the density (or temperature) fluctuations is consistent with the convective saturation limit of the linear theory for wavelengths up to 3 or 4 km in the lower mesosphere, and up to 6 km above 60 km altitude. Furthermore, convective unstable layers, which could persist over periods larger than one hour, are currently observed in the mesosphere.

Because of the day-to-day variability of the waves energy density (which reaches a factor of 5 in the stratosphere, and 1 order of magnitude in the mesosphere) a large data set must be analyzed in order to give a general view of the wave activity in this height range. This is the subject of the companion paper which will describe and discuss the gravity wave climatology from the large data set obtained by Rayleigh lidars at the two sites.

References

Balsley, B. B. and R. Garello, The kinetic energy density in the troposphere, stratosphere and mesosphere: A preliminary study using the Poker Flat MST radar in Alaska, Radio. Sci., 20, 1355-1361, 1985.

Barat, J., Initial results from the use of ionic anemometers under stratospheric balloons: Application to the high-resolution analysis of stratospheric motions, J. Appl. Meteorol., 21, 1489-1496, 1982.

Chanin, M. L., and A. Hauchecorne, Lidar observation of gravity and tidal waves in the stratosphere and mesosphere, J. Geophys. Res., 86, 9715-9721, 1981.

Chanin, M. L., and A. Hauchecorne, Lidar studies of temperature and density using Rayleigh scattering, MAP Handbook, 13, edited by R. A. Vincent, pp. 87-99, SCOSTEP, Urbana, Illinois, 1984.

Cot, C., and J. Barat, Wave turbulence interaction in the stratosphere: A case study, J. Geophys. Res., 91, 2749-2756, 1986.

Dewan, E. M., and R. E. Good, Saturation and the "universal" spectrum for vertical profile of horizontal scalar winds in the stratosphere, J. Geophys. Res., 91, 2742-2748, 1986.

Dewan, E. M., N. Grossbard, A. F. Quesada, and R. E. Good, Spectral analysis of 10 m resolution scalar velocity profiles in the stratosphere, Geophys. Res. Lett., 11, 80-83, 1984 (Correction, Geophys. Res. Lett., 11, 624, 1984).

Eckermann, S. D., and R. A. Vincent, Falling sphere observations of anisotropic wave motions in the upper stratosphere over Australia, Pure and Appl. Geophys., 130, 509-532, 1989.

Fritts, D. C., Gravity wave saturation in the middle atmosphere: A review of theory and observations, Rev. Geophys. Space Phys., 22, 275-308, 1984.

Fritts, D. C., and P. K. Rastogi, Convective and dynamical instabilities due to gravity wave motions in the lower and middle atmosphere: Theory and observation, Radio Sci., 20, 1247-1278, 1985.

Fritts, D. C., T. Tsuda, T. Sato, S. Fukao, S. Kato; Observational evidence of a saturated gravity wave spectrum in the troposphere and lower stratosphere, J. Atmos. Sci., 45, 1741-1759, 1988.

Garcia, R. R., and S. Solomon, The effects of breaking gravity waves on the dynamical and chemical composition of the mesosphere and lower thermosphere, J. Geophys. Res., 90, 3850-3858, 1985.

Gardner, C. S., M. S. Miller, and C. H. Liu, Rayleigh lidar observations of gravity wave activity in the upper stratosphere at Urbana, Illinois, J. Atmos. Sci., 46, 1838-1854, 1989.

Garrett, C. J. R., and W. H. Munk, Space-time scales of

internal waves, A progress report, J. Geophys. Res., 80, 291-297, 1975.

Gossard, E. E., and W. H. Hooke, Waves in the Atmosphere, Elsevier, New York, 1975.

Hass, H., and W. Meyer, Gravity wave field above Andøya, J. Atmos. Terr. Phys., 49, 705-712, 1987.

Hauchecorne, A., and A. Maillard, A 2D dynamical model of mesospheric temperature inversions in winter, Geophys. Res. Lett., 17, 2197-2200, 1990.

Hauchecorne, A., and M. L. Chanin, Density and temperature profiles obtained by lidar between 35 and 70 km, Geophys. Res. Lett., 7, 565-568, 1980.

Hauchecorne, A., M. L. Chanin, and R. Wilson, Mesospheric temperature inversion and gravity wave breaking, Geophys. Res. Lett., 14, 933-936, 1987.

Hirota, I., Climatology of gravity waves in the middle atmosphere, J. Atmos. Terr. Phys., 46, 767-773, 1984.

Hirota, I., and T. Niki, A statistical study of inertia gravity waves in the middle atmosphere, J. Meteorol. Soc. Jpn., 63, 1055-1066, 1985.

Holton, J. R., The role of gravity wave-induced drag and diffusion in the momentum budget of the mesosphere, J. Atmos. Sci., 39, 791-799, 1982.

Kundu, P. K., An analysis of inertial oscillations observed near Oregon coast, J. Phys. Oceanogr., 6, 879-893, 1976.

Lindzen, R. S., Turbulence and stress due to gravity wave and tidal breakdown, J. Geophys. Res., 86, 9707-9714, 1981.

Mathews, J. D., J. K. Berakall, and G. K. Karawas, The discrete prolate spheroidal filter as a digital signal processing tool, MAP Handbook, 9, edited by S. A. Bowhill and B. Edwards, pp. 563-571, SCOSTEP, Urbana, Illinois, 1983.

Meek, C. E., I. M. Reid, and A. H. Manson, Observation of mesospheric wind velocities, Cross sections of power spectral density for 48-8 hours, 8-1 hours, and 1 hour to 10 mn over 60-110 km for 1981, Radio Sci., 20, 1363-1382, 1985.

Miyahara, S., Y. Hayashi, and J. D. Mahlman, Interactions between gravity waves and the planetary scale flow simulated by the GFDL "SKYHI" general circulation model, J. Atmos. Sci., 43, 1844-1861, 1986.

Murgatroyd, R. J., and F. Singleton, Possible meridional circulations in the stratosphere and mesosphere, Q. J. R. Meteorol. Soc., 87, 125-135, 1961.

Nastrom, G. D., and K. S. Gage, A climatology of atmospheric wave number spectra observed by commercial aircraft, J. Atmos. Sci., 42, 950-960, 1985.

Palmer, T. N., G. J. Shutts, and R. Swinbanck, Alleviation of a systematic westerly bias in general circulation and numerical weather prediction through an orographic gravity wave drag parameterization, Q. J. R. Meteorol. Soc., 112, 1001-1040, 1986.

Shibata, T., T. Fukuda, and M. Maeda, Density fluctuations in the middle atmosphere over Fukuoka observed by an XeF Rayleigh lidar, Geophys. Res. Lett., 13, 1121-1124, 1986.

Shibata, T., S. Ichimori, T. Narikiyo, and M. Maeda, Spectral analysis of vertical temperature profiles observed by a lidar in the upper stratosphere and the lower mesosphere, J. Meteorol. Soc. Jpn., 66, 1001-1005, 1988.

Sidi, C., J. Lefrère, F. Dalaudier, and J. Barat, An improved atmospheric buoyancy wave spectrum model, J. Geophys. Res., 93, 774-790, 1988.

Smith, S. A., D. C Fritts, and T. E. Van Zandt, Evidence for a saturated spectrum of atmospheric gravity waves, J. Atmos. Sci., 44, 1404-1010, 1987.

Tsuda, T., T. Inoue, D. C. Fritts, T. E. Van Zandt, S. Kato, T. Sato, and S. Fukao, MST radar observation of a saturated gravity wave spectrum, J. Atmos. Sci., 46, 2440-2447, 1989.

VanZandt , T. E., A universal spectrum of buoyancy waves in the atmosphere, Geophys. Res. Lett., 9, 575-578, 1982.

Vincent, R. A., Gravity wave motion in the mesosphere, J. Atmos. Terr. Phys., 46, 119-128, 1984.

Vincent, R. A., and D. C. Fritts, A climatology of gravity wave motion in the mesopause region at Adelaide, Australia, J. Atmos. Sci., 44, 748-760, 1987.

M. L. Chanin, A. Hauchecorne and R. Wilson, Service d'Aéronomie du CNRS, 91373 Verrières le Buisson Cedex, France.

(Received November 2, 1989;
revised August 28, 1990;
accepted October 11, 1990.)